Revealing Exciton and Metal-Ligand Conduction Band Charge Transfer Absorption Spectra in Cu-Zn-In-S Nanocrystals

Brener R. C. Vale,[†§] Etienne Socie,[†] Leticia R. C. Cunha,[§] Andre F. V. Fonseca,[§] Roberto Vaz,[§] Jefferson Bettini,[‡] Jacques-E. Moser,[†] and Marco A. Schiavon[§*]*

[†] Photochemical Dynamics Group, Institute of Chemical Sciences & Engineering, École Polytechnique Fédérale de Lausanne, CH-1015 Lausanne, Switzerland

[§] Grupo de Pesquisa Química de Materiais, Departamento de Ciências Naturais, Universidade Federal de São João Del-Rei, Campus Dom Bosco, 36301-160 São João Del-Rei, Minas Gerais, Brazil

[‡] Laboratório Nacional de Nanotecnologia, Centro Nacional de Pesquisa em Energia e Materiais, Campinas, São Paulo, Brazil

Corresponding Authors

* je.moser@epfl.ch (J.-E. Moser)

* schiavon@ufsj.edu.br (M.A. Schiavon)

ABSTRACT

Heavy metal-free semiconductor nanocrystals such as copper indium sulfide quantum dots (QDs) have attracted substantial attention in recent years due to environmental issues and diverse applications. We report the synthesis and characterization of copper-zinc-indium-sulfide (CZIS) QDs and CZIS treated with excess Zn^{2+} at different temperatures, denoted here as CZIS/ZnS 100 and CZIS/ZnS 200. Zn^{2+} can diffuse into the lattice by an exchange-cation reaction, replacing Cu^{+} and In^{3+}. We employed transient absorption (TA) spectroscopy to study the role of Zn^{2+} in the lattice. The data were treated by global analysis, which yielded the decay associated spectra (DAS). Through DAS and second-order derivative absorption spectra, we could isolate the excitonic contribution from the metal ligand conduction band charge transfer ($ML_{CB}CT$) absorption in the TA spectrum, finding the hole localization lifetime by its spectral and dynamical features. The hole localization lifetime increases from 0.3 to 1.7 ps by increasing the Zn^{2+} concentration. We also measured the electron trapping constants to be 30 ps and larger than 1 ns. Finally, we concluded that the improvement in the photoluminescence quantum yield originates from accelerated radiative transition relative to the nonradiative component. A detailed mechanism was proposed, and our results suggest that the introduction of Zn^{2+} in the lattice of CIS QDs could be beneficial for charge extraction.

KEYWORDS: Copper zinc indium sulfide, quantum dots, transient absorption spectroscopy, decay associated spectra, cation-exchange reaction, global analysis, heavy metal-free.

Heavy metal-free semiconductor nanocrystals have been extensively studied due to environmental issues. Ternary semiconductors such as copper indium sulfide (CIS) quantum dots (QDs) have displayed very interesting optoelectronic properties for applications in photovoltaic devices,[1–3] LEDs,[4] and biomarkers.[5] CIS QD colloidal dispersions show long charge-carrier radiative recombination lifetimes (hundreds of nanoseconds), a large molar extinction coefficient from the visible to the near-infrared spectrum (10^5 L mol^{-1} cm^{-1}), and large Stokes shifts (~250 to 500 meV) free of reabsorption effects.[6,7] However, CIS QDs have a low photoluminescence quantum yield (PLQY) (< 10%) due to their large density of defects.[8,9] To overcome this limitation, core-shell structures have been proposed, and CIS core-shell QDs can typically achieve a high PLQY above 50%, depending on the shell composition and the experimental approach.[10,11]

The CIS QDs are usually shelled with a wider bandgap semiconductor, such as ZnS or CdS, by similar experimental approaches used for Cd and Pb chalcogenides QDs.[8,10,11] However, instead of a slight redshift in the absorption and emission spectra of the core-shell structure typically observed for type I core-shell alignments, a blueshift is observed in most cases. Some authors have ascribed the blueshift to alloying, cation-exchange, and etching processes.[10,12–14] Cation-exchange occurs upon adsorption of Zn-ligand species on the CIS QD surface. Thus, an exchange reaction can take place when Zn^{2+} cations are incorporated in the QD and Cu^{+} or In^{3+} cations are extracted as M-ligands species. Alloying is slightly different from cation-exchange; the former occurs when Zn^{2+} from ZnS adsorbed on the surface diffuses inward, while Cu^{+} or In^{3+} ions diffuse outward. Since both processes are quite similar, diverging just on the Zn^{2+} source, we interpreted the blueshift reported here by convention as a cation-exchange process. Cation-exchange with Zn^{2+} is also effective to increase the PLQY; for example, Lu *et al*. achieved with a record low fluence a two-photon amplified spontaneous emission (ASE) in Zn-processed CIS QDs.[14] Etching occurs

when species in the reaction medium promote the partial dissolution of the CIS QDs by extracting cations and/or S^{2-} from the lattice, decreasing the particle size. According to Donega's group, the redshift occurs only for heteroepitaxial shell overgrowth.[13] Moreover, they have demonstrated that the chemical route employed can control the different processes. Reactive precursors can promote the heteroepitaxy shell overgrowth, while nonreactive precursors promote cation-exchange or etching.[13]

To improve the optical properties of CIS QDs, it is critical to understand the mechanism involved in the electronic transition, since CIS QDs have different optical properties from those composed of CdL and PbL chalcogenides (L = S and Se), $CsPbX_3$ perovskites (X = Cl, Br, and I), *etc*. Many groups have devoted efforts to developing CIS QD optoelectronic properties, for example, to understand why the PL has a large Stokes shift, a broad emission band, and a long recombination lifetime. In the last 10 years, some proposals have been suggested to answer these questions, such as the forbiddances of optical transitions between the excited and ground states due to the tetragonal symmetry of the crystal lattice,[15] exciton self-trapping process,[16] and acceptor-donor pair states.[17] Recently, some publications have demonstrated experimentally predicted behaviors in the tetragonal symmetry of the crystal lattice.[18,19] However, the most accepted model suggested that the fluorescence comes from the recombination between the electrons delocalized in the conduction band (CB) and the confined hole state (CHS) due to the trap related to copper ions.[11,20,21] The same behavior has been observed for Zn and Cd chalcogenides intentionally doped with copper.[16,22–24] Berends, A. *et al*. proposed that the mechanism of electron-hole pair relaxation occurs in three steps – the first is hole localization on the CHS, which occurs in an ultrafast time-scale less than 100 fs. However, they do not show any experimental evidence of hole localization, such as spectral or dynamical features. The second one is divided into two competing processes,

which are electron trapping (recombination between the electron in the delocalized CB to electron traps) and radiative recombination between the electron in the delocalized CB and CHS, and the third one is the nonradiative recombination between the trapped electron and the CHS.[11]

The Cu-related defect oxidation state can also play an important role in the electronic properties of CIS. The Cu^{+} defect is absorption-active due to the excitation of one of its 3d electrons into the CB state, leaving the Cu cation in the $3d^9$ configuration.[20,25,26] This transition, called metal-to-ligand (conduction band) charge transfer ($ML_{CB}CT$), leads to intragap absorption, which contributes to the apparent broadening of the absorption edge. However, Cu^{+} emission needs prior activation, which requires the capture of a photoexcited VB hole. On the other hand, Cu^{2+} is absorption-inactive, since the transition from the electron in the $3d^9$ configuration cannot be transformed into the $3d^8$ configuration by excitation of one electron into the CB.[25] Therefore, Cu^{2+} defects do not contribute to the CIS absorption spectrum. Although Cu^{2+} absorption is inactive, it is "emission-ready", since the electron in the CB can directly recombine with the electron vacancy in the 3d shell. In addition, the photoexcited VB hole can provide fast Auger recombination due to the three-particle (VB hole, Cu^{2+} hole, and CB electron) recombination process.[25,27] Thus, Cu^{2+}-related defect emission requires the absence of this Auger process, which could be done by the fast removal of the VB hole due to trapping in a non-Cu^{+}-related defect; otherwise, Cu^{2+} will be in a "dark" state.

The composition can also control the Cu-related defect on CIS QDs. Because of charge compensating arguments, for stoichiometric samples with a 1:1 Cu-to-In ratio, the prevailing defects are an antisite pair of Cu^{+} cations sitting on an In^{3+} lattice site with a double negative charge and an In^{3+} cation sitting on a Cu^{+} lattice site with a double positive charge, as denoted in the Kröger-Vink notation of crystallographic defects represented as Cu_{In}''-$In_{Cu}^{\cdot\cdot}$. On the other hand,

copper deficiency leads to Cu vacancies (v_{Cu}'), which in turn will facilitate the creation of charge compensating Cu^{2+} defects ($Cu_{Cu}^{\cdot}$). These observations are supported by magneto-optical measurements.[25]

However, some questions are still unanswered in the literature: if the hole localizes at the CHS in a ultrafast time scale and the $ML_{CB}CT$ transition has a lower probability transition than the excitonic one, is it possible to use TA spectroscopy to experimentally measure the exciton absorption spectrum before hole localization and the free $ML_{CB}CT$ transition? Why does the TA spectrum not well overlap with the second-order derivative absorption spectra? How can the excitonic and $ML_{CB}CT$ transitions be influenced by Zn^{2+} incorporation? In this work, we report the synthesis and characterization of copper-zinc indium sulfide (CZIS) QDs and CZIS treated with excess Zn^{2+} at 100 and 200 ºC. We have employed ultrafast TA spectroscopy to answer the questions aforementioned.

Results and Discussion

We prepared three different samples labeled here as CZIS, CZIS-ZnS 100, and CZIS-ZnS 200 according to a previous report in the literature with slight modifications (see the method section for details).[28] Figure 1a shows the PL and UV-Vis spectra (solid and dashed line, respectively) of the three prepared samples. The absorption spectra for all the samples were normalized at 390 nm (3.2 eV) or their spectral shape was considered for comparison. The absorption band of the three samples is featureless, which is very common for CIS QDs. The featureless absorption spectrum comes from the size and composition (Cu:In) distribution in the ensemble. Furthermore, Gamelin's group has demonstrated that even NCs with identical sizes and compositions but with different Cu^{+} and In^{3+} spatial positions can change the HOMO and LUMO energy level by as much as 1 eV, contributing for the inhomogeneous broadening of the spectroscopic properties.[29] To measure

the VB-CB exciton band-edge ($h\nu_x$) transition, we used the second-order derivative of the absorption spectrum (SODAS), a usual procedure used in the literature for featureless absorption spectra, as shown in Figure 1b. The calculated $h\nu_x$ transition through SODAS was summarized in Table S1. After Zn^{2+} incorporation, the temperature increases $h\nu_x$, and the PL spectra shift to higher energies. This behavior is typical for CIS QDs and is due to cation-exchange processes, in which In^{3+} and Cu^{+} are replaced by Zn^{2+} in the lattice structure. The increase in the temperature facilitates the diffusion of Zn^{2+} into the lattice. Moser *et al*. conducted *in situ* PL measurements to control cation-exchange reaction shell growth on CISe NCs.[30] They concluded that the cation-exchange growth mechanism consists of a surface reaction of the Zn precursor, followed by the sequential solid-state diffusion of Zn^{2+} atoms into successive atomic monolayers.[30] Density of states (DOS) studies explain the blueshift in the absorption and emission spectra: according to DOS, the Cu^{+} and S^{-2} orbitals contribute to the VB-edge, while In^{3+} and Cu^{+} contribute to the CB-edge for CIS QDs. When the Zn^{2+} concentration increases in the alloy (CZIS) QDs, Zn^{2+} (3d) orbitals also start to contribute to the CB-edge, which gradually shifts into higher energies.[29] We also observed that the intragap absorption $ML_{CB}CT$ band, with absorption of approximately 600 nm (2.1 eV), progressively decreases from CZIS to CZIS/ZnS 200, and the explanation for this observation will be discussed later with the TA results. The PL maximum, exciton transition energy, and the apparent Stokes shift were summarized in Table 1S in the supporting information. However, we cannot exclude the formation of a thin layer of a ZnS shell, because we observed a substantial increase in the PLQY of the samples treated with Zn^{2+} at 100 and 200 ºC compared to the PLQY of the CZIS sample. CZIS, CZIS/ZnS 100, and CZIS/ZnS 200 shows a PLQY of 12, 17, and 54%, respectively.

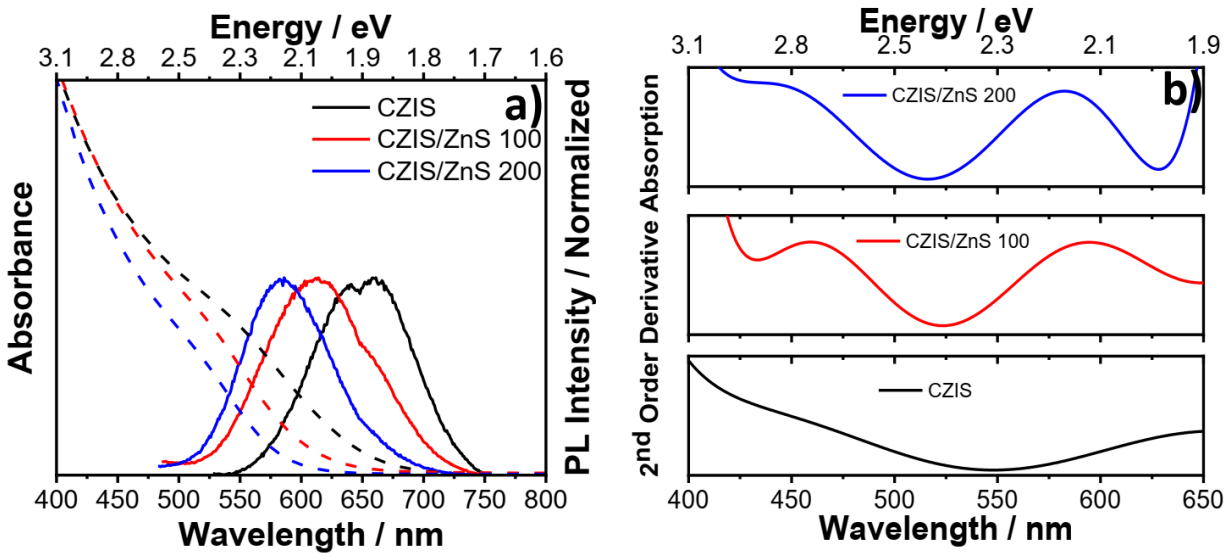

Figure 1. a) Absorption (dashed line) and photoluminescence (straight line) spectra. b) Second order derivative of the absorption of CZIS, CZIS/ZnS 100, and CZIS/ZnS 200 QDs.

We carried out ultrafast TAS to measure the relaxation of the photoexcited species in CZIS QDs. The setup was previously described in another paper, and details can be found in the SI.[31] We have excited the samples with a pump pulse centered at 500 nm with pulse duration and a full width at half maximum (FWHM) of approximately 50 – 60 fs and probed with a white beam in the region between 400 – 780 nm; see the supporting information (SI) for more details. The TA spectrum of the CIS QDs is interpreted as the depopulation of electrons in the lowest-energy delocalized CB state;[11] moreover, TAS measurements have shown that this state is two-fold degenerated.[11,32] We have measured the absorption cross-section at 390 nm (3.2 eV) ($\sigma_{3.2\ eV}$), and we noticed that $\sigma_{3.2\ eV}$ did not change considerably from CZIS to CZIS-ZnS QDs treated at 100 or 200 ºC, as shown in Fig. 1S. We have found absorption cross-section values close to the ones reported by Nagamine *et al.*[18] Since $\sigma_{3.2\ eV}$ is proportional to the particle volume, the particle size did not change, excluding the contribution of the etching process to the blueshift in the emission and absorption spectra (see SI).[18]

Fig. 2 shows the TA spectra of CZIS, CZIS/ZnS 100, and CZIS/ZnS 200. In these measurements, we have used ~ 7.7 x 10^{14} photons cm^{-2}, corresponding to an average of 0.3 excitons per particle. The average number of excitons per QD ($<N_x>$) was calculated by the equation $<N_x> = j\sigma_{2.48ev}$, where j is the density of photons, and $\sigma_{2.48ev}$ is the absorption cross-section at 2.48 eV; see the SI for details. The TA spectrum obtained at 1 ps for different photon fluences has the same shape in the range of ~0.05 to 0.3 $<N_x>$, suggesting that the effect of biexcitons on the spectral features is negligible, as shown in Fig. 3S. Moreover, the normalized bleach decay showed the same decay rate in this range as shown by photofluences, which means that the multiexcitonic processes are also negligible, as shown in Fig. 4S.

The TA spectrum is composed of ground state bleach (GSB) and a broad photoinduced absorption (PIA) bands, as reflected by the negative and positive peaks, respectively. We observed that the GSB is slightly redshifted compared to the $h\nu_x$ measured by the SODAS for all the systems studied here. Fig. 5S shows the comparison of the TA, UV-Vis, and PL spectra. The GSB in semiconductor QDs is usually centered close to the ground state absorption; even for CdSe QDs that are intentionally doped with copper ions, this redshift does not occur in the GSB. The redshifted GSB for CIS QDs could be ascribed to the average of the two main processes, which are a VB-CB excitonic transition ($h\nu_{x,ta}$) and intragap absorption due to the $ML_{CB}CT$ transition ($h\nu_{cu}$). Klimov's group has recently carried out a study comparing two samples differing in copper contents but with similar size distributions. The SODAS for both samples is overlapped and has minimums located at 2.25 eV. The TA spectrum of the stochiometric CIS QDs is different from that of the poor copper one in terms of shape and spectral energy. The deficient copper QDs showed two bands: a sharp one close to the intrinsic VB-CB excitonic transition ($h\nu_{x,ta}$) at 2.21 eV (40 meV redshifted compared to the $h\nu_x$ measured by the SODAS) and another one located at 2.02

eV, which is ascribed to $h\nu_{cu}$. For the stochiometric sample, just one broadband was centered at 2.04 eV (210 meV redshifted compared to $h\nu_x$), which is ascribed to $h\nu_{Cu}$. Klimov's group also noticed that the dynamic of the peak located at 2.21 eV has a short-lived component with a time constant of 1.4 ps, which is absent for the stochiometric sample. They attributed this short-lived component to hole localization. The GSB minimums for the samples studied here were summarized in Table S2. As seen from this table, the energy difference between the minimum of the GSB and the $h\nu_x$ for our samples is in the range of 97 to 63 meV, decreasing from CZIS to CZIS/ZnS 200. These results are slightly greater than the energy difference between $h\nu_x$ and $h\nu_{x,TA}$ (40 meV) and less than the energy difference between $h\nu_{x\ and}$ $h\nu_{Cu}$ (210 meV) found by Klimov's group.

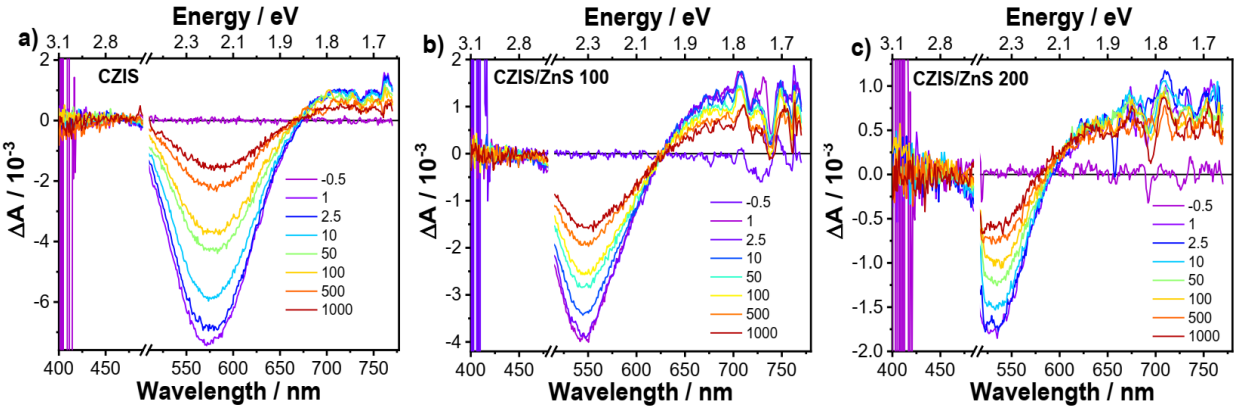

Figure 2. TA spectra showing different slices for a) CZIS, b) CZIS/ZnS 100, and c) CZIS/ZnS 200.

Since the GSB signal for CIS QDs is complex, we examined the GSB decay at different energies. Fig. 6S shows the dynamics for different energies around the GSB for the three samples studied here. The dynamics were integrated into five nanometers around the selected probed energy to increase the signal-to-noise ratio. We selected energies as close as possible to $h\nu_x$ and at lower

energies to detect the contribution of the $ML_{CB}CT$ transition. The dynamics probed at different energies showed complex behaviors. For instance, we observed that the dynamics probed at a higher energy decay was faster than the dynamics at a lower energy for the CZIS QD sample. To obtain useful information from these data, we have used global analysis to extract the dynamic and spectral behavior from the different samples; see the SI for details.

Fig. 3 shows the decay associated spectra (DAS) obtained from the global analysis pumped at 390 nm. The DAS shows the amplitude of a specific decay as a function of the corresponding wavelength. The difference between the DAS spectrum and the directly measured TA spectrum is that the former is calculated just based on the amplitude of the component decay, while the latter is based on the intensity of the signal, which depends on the concentration, oscillator strength, and decay. Thus, the low signal at a specific region in the experimental spectrum due to a low concentration or low oscillator strength can be hidden in a normal spectrum. Therefore, signals that are low but with steep decay will be pronounced in DAS. The positive amplitude in DAS comes from a positive signal that decays over time or is due to a negative signal with an ultrafast timescale rise, while the negative amplitude just comes from negative signal decay. For all samples, we observed triexponential decay. Only for the samples excited at 500 nm, we have used a triexponential function plus an offset. All time-constants for the different samples can be found in the Tables 3S and 4S. The different time-constants observed when pumped at 390 or 500 nm come from the large difference between the pulse width durations for the pump pulses at 390 (~ 350 fs) and 500 nm (~ 60 fs), and because of that, the intervals for data fitting were also different; see the SI for details. We observed that the GSB obtained from the DAS (GSB_{DAS}) is shifted to a lower energy as the time-constant increases from A1 to A3. For samples pumped at 500 nm, we could not properly measure the dynamics probed approximately 500-510 nm for CZIS/ZnS 100

and CZIS/ZnS 200 QDs due to the strong scattering from the pump; see Figure 5S. Because of that, the minimum of the A1 components for these samples could not be seen in Fig. 7S. We can say that our results when pumped at 390 nm are rich in terms of spectral resolution but poor in terms of time resolution; however, the samples pumped at 500 nm are rich in terms of time resolution but poor in terms of spectral content.

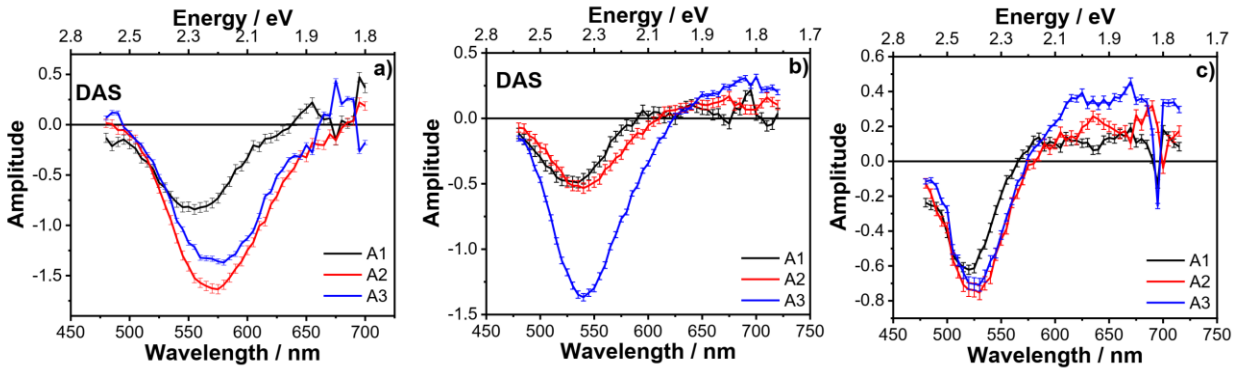

Figure 3. Decay associated spectra (DAS) pumped at 390 nm for a) CZIS, b) CZIS/ZnS 100, and c) CZIS/ZnS 200.

Interestingly, we observed that the minimum of the A1 component for all the samples matches very well with the $h\nu_x$ measured by SODAS, and Table 1 summarizes all these values. The DAS have been used for other semiconductors, and usually, the fastest component, denoted here as A1, has been ascribed to cooling prior to relaxation to the band-edge. Moreover, the time-constant related to cooling on the CIS QDs is on the order of hundreds of femtoseconds when pumped at 3.1 eV or even slower (~2 ps) under a high photofluence ($\langle N_x \rangle$ ~4.0). [33,34] Nevertheless, we can exclude the possibility of cooling in this work because of two reasons: first, the time-constants found here were greater than 4 ps for all cases when excited at 390 nm and longer than 300 fs when

excited at 500 nm at a low fluence ($<N_x>$ ~0.3). When we applied excitation at 500 nm, we could still have some contribution from cooling only for the CZIS sample because of the extra energy and the time constant, which can explain why the minimum for the "GSB" is blueshifted compared to the one pumped at 390 nm. When excited at 390 nm, we assume that the spectra for all cases cannot encompass a cooling process because of our poor time-resolution and the constraints used in the fitting procedure. Second, when we pumped at 500 nm, we would not expect cooling for CZIS/ZnS 200, because excitation is almost resonant. We can see an A1 "GSB" blueshifted compared to A2 and A3, which suggest that this signal is due to excitonic bleaching. In addition, if the signal in A1 comes from cooling, we expect a decrease in the time constant from CZIS to CZIS/ZnS 200 QDs, because the extra energy decreases in this series, but the result is contrary to that. Thus, cooling is not the process observed here. Therefore, our results reported can be seen in the following way: after photoexcitation, the exciton is created and remains delocalized (i.e., the electron is delocalized into the CB, and the hole is delocalized into the VB) for a specific time, which depends on the Zn concentration. This explains why the GSB_{DAS} matches very well with the $h\nu_x$ measured by SODAS. Later, the hole is trapped in a CHS, shifting the GSB_{DAS} minimum to a lower energy and broadening its shape.

From now, we will concentrate on the fastest time-constant (A1 component). When we pumped the samples at 500 nm, we noticed that the time-constant of the A1 component increases from CZIS to CZIS/ZnS 200 QDs, and the same is observed when pumped at 390 nm, as shown in Tables S3 and S4, respectively. Since an increase in the time-constant means a decrease in the probability of recombination, these results suggested that the hole localization rate decreases when more Cu^+ and In^{3+} are replaced by Zn^{2+} through the cation-exchange reaction. Klimov's group has recently reported a hole localization of 1.4 ps for CIS QDs when pumped at 355 nm. Donega's

group have suggested hole localization of fewer than 100 fs when pumped at 500 nm.[11] Note that the samples investigated in these studies are almost stochiometric CIS QDs ($[Cu^+]/[In^{3+}] \sim 1$), indicating that this hole localization is faster than the process presented by our results, which makes sense with the trends presented here, since increasing the Zn^{2+} content increases the time-constant. However, apart from Klimov's group, other studies have not shown experimental evidence of hole localization, such as spectral or dynamical features.

Table 1. $h\nu_x$ and "GSB" energy minimum measured by the SODAS and DAS approaches, respectively

Samples	$h\nu_x$/eV/nm	A1/eV/nm	A2/eV/nm	A3/eV/nm
CZIS	2.254/550	2.234/555	2.156/575	2.138/580
CZIS/ZnS 100	2.371/523	2.339/530	2.296/540	2.296/540
CZIS/ZnS 200	2.403/516	2.384/520	2.339/530	2.339/530

* The error of the wavelength is ± 2 nm

As we mentioned earlier, TA spectrum bleaching is composed of excitonic and $ML_{CB}CT$ transitions. We also noticed that the FWHM of the TA spectrum decreases, and the shift in the "GSB" minimum in the DAS decreases from A1 in CZIS to A3 in CZIS/ZnS 200 (Table 2), which can be related to the suppression of the $ML_{CB}CT$ transition owing to the decrease in the Cu^+ concentration. As we mentioned above, we have noticed that the linear absorption spectra of CZIS/ZnS 100 and 200 QDs are sharper than those of CZIS QDs (Fig. 2S). We observed that the FWHM obtained from the TA spectra does not change significantly over time (the result is not

shown) due to the low sensitivity of low signals, as we explained earlier. Thus, the specific time is not important here, and we used the spectra at 1 ps because of the high signal-to-noise ratio. Therefore, the sharper absorption spectra and larger time constants found for CZIS/ZnS 100 and 200 suggested that Zn^{2+} decreases the concentration of Cu^{+} and In^{3+}, which decreases the contribution of $ML_{CB}CT$ absorption to the absorption spectrum, decreasing the hole localization rate. Therefore, the longer hole localization lifetime with increasing Zn^{2+} could be easier for hole extraction, since this process will be more competitive with the hole localization.

According to the time constant and spectral signatures found for A2 and A3 obtained from DAS, we can say that A2 and A3 are related to electron trapping.[10,11,35] Nevertheless, due to the limitation of our delay line, we could measure the dynamics only until 1880 ps, and thus, the time constant reported for the A3 component is just an approximation that we observed for long-lived decay. We noticed that the electron trapping process is much faster for CZIS than for CZIS/ZnS 100 or 200, but there is not much difference between the electron trapping processes of CZIS/ZnS treated at 100 or 200 ºC. This outcome suggests that Zn^{2+} incorporation is also effective to remove traps, making these materials interesting for applications such as LEDs and photovoltaic devices.

Table 2. FWHM for the A1 and A3 component from the DAS and TA spectrum

Samples	A1 FWHM/nm	A3 FWHM/nm	TA* FWHM/nm
CZIS	75	85	85
CZIS/ZnS 100	67	73	70
CZIS/ZnS 200	48	51	55

* The TA spectrum collected at 1 ps

Finally, we carried out PL time-resolved measurements by a time-correlated single photon counting (TCSPC) technique to measure the full relaxation process in the materials. The PL decay

curves are shown in Figure 7S. We monitored the PL decay at the maximum of the PL spectrum. The emission decay is multiexponential and can be fitted to a biexponential function. Table S5 shows the time-constants and respective amplitudes. The average PL lifetime was calculated through Equation S7. According to the average PL lifetime and PLQY relationship, we could separate the radiative and nonradiative decay lifetimes. Since the radiative and nonradiative lifetime were much longer than the time-constants found by the TA measurements, we can say that radiative and nonradiative rates do not contribute to the TA signals. Berends *et al*. also concluded that previously.[11] As seen from Fig. 8S, the PL decay curve did not increase upon Zn^{2+} cation-exchange. Since the PLQY increase from CZIS to CZIS-ZnS 200, we can say that the improvement in the PLQY is due to the increase in the radiative decay rate compared to that of the nonradiative one.

We have proposed a mechanism for this work, which is the following: since the probability of the $ML_{CB}CT$ transition is much lower than that of the excitonic one, we can say that the first process to occur is excitonic recombination; additionally, the GSB_{DAS} observed for A1 accounted just for excitonic absorption, and the time constant is related to hole localization. Because of efficient hole localization, which relaxes the exciton and localizes the hole into the CHS located a few meV above the VB, the electron will recombine with the hole at the CHS, and the A2 GSB_{DAS} is redshifted compared to A1. The time constants related to A2 and A3 are related to the electron trapping process. The radiative and nonradiative recombination processes take a very long time, longer than 100 ns, and do not contribute to the ultrafast TA spectrum. Radiative recombination comes from an electron in the delocalized CB and hole in the CHS. However, nonradiative recombination comes from the electron trapped and the hole in the CHS. Scheme 1 shows a representation of the mechanism proposed in this work.

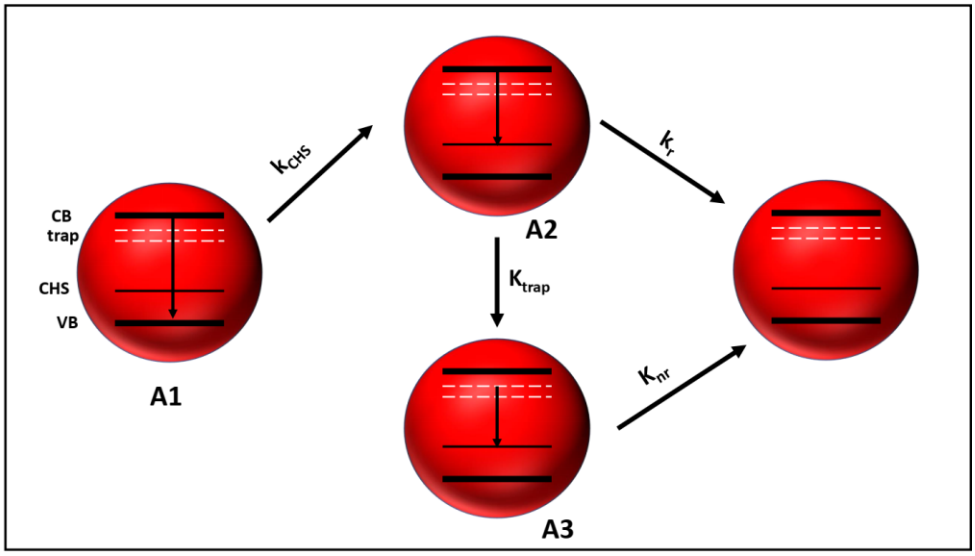

Scheme 1. The mechanism proposed in this work (see the main text).

Conclusion

Therefore, we have shown that increasing the Zn^{2+} concentration in the lattice shifts absorption and PL to higher energies. The cation-exchange process is also accompanied by a thin ZnS shell layer, which increase the PLQY. Our methodology based on DAS obtained from TAS has spectral and dynamically shown the exciton transition and hole localization, matching very well with the SODAS for all three samples studied here. In addition, we have shown the time constant related to hole localization is dependent on the Zn concentration, becoming less efficient for larger concentrations of Zn^{2+}. The electron trapping process decreases when CZIS QDs reacted with excess Zn^{2+}. Note that suppression of the electron trapping rate is not the only process responsible for increasing the PLQY, as it also increases the radiative recombination rate. Our results suggest that the introduction of Zn^{2+} in the lattice of CIS QDs could be interesting for LEDs and photovoltaic applications.

ASSOCIATED CONTENT

Supporting Information

The supporting information is available free of charges on the ACS Publications website at DOI:

Methods, global analysis, absorption cross-section measurements, PL maximum and second order derivative absorption minimum, TA bleach minimum and true Stokes shift, dependence of TA bleaching on the photon fluence, estimated absorption cross-section wavelength dependence, TA spectra normalized at 1 ps and GSB decay at different photon fluences, decay curves probed at different energies, DAS pumped at 500 nm, time-constants for DAS pumped at 500 and 390 nm, PL decay curve obtained from TCSPC.

AUTHOR INFORMATION

ORCID

Brener R. C. Vale: 0000-0002-2047-5965

Jacques-E. Moser: 0000-0003-0747-4666

Marco A. Schiavon: 0000-0002-1553-5388

Author Contributions

The manuscript was written through contributions of all the authors. All the authors have given approval to the final version of the manuscript.

Notes

The authors declare no competing financial interests.

ACKNOWLEDGMENT

Financial support by the Swiss National Science Foundation (SNF), NCCR-MUST (a research instrument of the SNF), the Swiss Confederation through a Swiss Government Excellence

Scholarship, CAPES, CNPq, and the Federal University of São João del-Rei are gratefully acknowledged.

TOC Figure

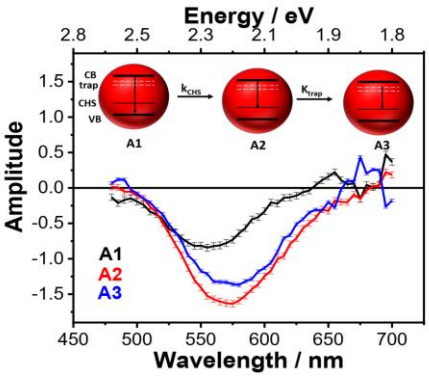

REFERENCES

(1) Du, J.; Du, Z.; Hu, J. S.; Pan, Z.; Shen, Q.; Sun, J.; Long, D.; Dong, H.; Sun, L.; Zhong, X.; et al. Zn-Cu-In-Se Quantum Dot Solar Cells with a Certified Power Conversion Efficiency of 11.6%. *J. Am. Chem. Soc.* **2016**, *138*, 4201–4209. https://doi.org/10.1021/jacs.6b00615.

(2) Chiang, Y. H.; Lin, K. Y.; Chen, Y. H.; Waki, K.; Abate, M. A.; Jiang, J. C.; Chang, J. Y. Aqueous Solution-Processed off-Stoichiometric Cu-In-S QDs and Their Application in Quantum Dot-Sensitized Solar Cells. *J. Mater. Chem. A* **2018**, *6*, 9629–9641. https://doi.org/10.1039/c8ta01064a.

(3) Santos, C. I. L.; Machado, W. S.; Wegner, K. D.; Gontijo, L. A. P.; Bettini, J.; Schiavon, M. A.; Reiss, P.; Aldakov, D. Hydrothermal Synthesis of Aqueous-Soluble Copper Indium Sulfide Nanocrystals and Their Use in Quantum Dot Sensitized Solar Cells. *Nanomaterials*

2020, *10*, 1–14. https://doi.org/10.3390/nano10071252.

(4) Boonsin, R.; Barros, A.; Donat, F.; Boyer, D.; Chadeyron, G.; Schneider, R.; Boutinaud, P.; Mahiou, R. Optical Properties and Reliability Studies of Gradient Alloyed Green Emitting (CdSe)x(ZnS)1-x and Red Emitting (CuInS2)x(ZnS)1-x Quantum Dots for White Light-Emitting Diodes. *ACS Photonics* **2018**, *5*, 462–470. https://doi.org/10.1021/acsphotonics.7b00980.

(5) Chetty, S. S.; Praneetha, S.; Vadivel Murugan, A.; Govarthanan, K.; Verma, R. S. Human Umbilical Cord Wharton's Jelly-Derived Mesenchymal Stem Cells Labeled with Mn2+ and Gd3+ Co-Doped CuInS2-ZnS Nanocrystals for Multimodality Imaging in a Tumor Mice Model. *ACS Appl. Mater. Interfaces* **2020**, *12*, 3415–3429. https://doi.org/10.1021/acsami.9b19054.

(6) Berends, A. C.; Mangnus, M. J. J.; Xia, C.; Rabouw, F. T.; De Mello Donega, C. Optoelectronic Properties of Ternary I-III-VI 2 Semiconductor Nanocrystals: Bright Prospects with Elusive Origins. *J. Phys. Chem. Lett.* **2019**, *10*, 1600–1616. https://doi.org/10.1021/acs.jpclett.8b03653.

(7) Xia, C.; Wu, W.; Yu, T.; Xie, X.; Van Oversteeg, C.; Gerritsen, H. C.; De Mello Donega, C. Size-Dependent Band-Gap and Molar Absorption Coefficients of Colloidal CuInS2 Quantum Dots. *ACS Nano* **2018**, *12*, 8350–8361. https://doi.org/10.1021/acsnano.8b03641.

(8) Leach, A. D. P.; Macdonald, J. E. Optoelectronic Properties of $CuInS_2$ Nanocrystals and Their Origin. *J. Phys. Chem. Lett.* **2016**, *7*, 572–583. https://doi.org/10.1021/acs.jpclett.5b02211.

(9) Jara, D. H.; Stamplecoskie, K. G.; Kamat, P. V. Two Distinct Transitions in CuxInS2 Quantum Dots. Bandgap versus Sub-Bandgap Excitations in Copper-Deficient Structures. *J. Phys. Chem. Lett.* **2016**, *7*, 1452–1459. https://doi.org/10.1021/acs.jpclett.6b00571.

(10) Bose, R.; Ahmed, G. H.; Alarousu, E.; Parida, M. R.; Abdelhady, A. L.; Bakr, O. M.; Mohammed, O. F. Direct Femtosecond Observation of Charge Carrier Recombination in Ternary Semiconductor Nanocrystals: The Effect of Composition and Shelling. *J. Phys. Chem. C* **2015**, *119*, 3439–3446. https://doi.org/10.1021/acs.jpcc.5b00204.

(11) Berends, A. C.; Rabouw, F. T.; Spoor, F. C. M.; Bladt, E.; Grozema, F. C.; Houtepen, A. J.; Siebbeles, L. D. A.; De Mello Donegá, C. Radiative and Nonradiative Recombination in CuInS2 Nanocrystals and CuInS2-Based Core/Shell Nanocrystals. *J. Phys. Chem. Lett.* **2016**, *7*, 3503–3509. https://doi.org/10.1021/acs.jpclett.6b01668.

(12) Zaiats, G.; Kinge, S.; Kamat, P. V. Origin of Dual Photoluminescence States in ZnS-CuInS2 Alloy Nanostructures. *J. Phys. Chem. C* **2016**, *120*, 10641–10646. https://doi.org/10.1021/acs.jpcc.6b01905.

(13) Berends, A. C.; Van Der Stam, W.; Hofmann, J. P.; Bladt, E.; Meeldijk, J. D.; Bals, S.; De Mello Donega, C. Interplay between Surface Chemistry, Precursor Reactivity, and Temperature Determines Outcome of ZnS Shelling Reactions on CuInS2 Nanocrystals. *Chem. Mater.* **2018**, *30*, 2400–2413. https://doi.org/10.1021/acs.chemmater.8b00477.

(14) Lu, P.; Li, R.; Yao, N.; Dai, X.; Ye, Z.; Zheng, K.; Kong, W.; Fang, W.; Li, S.; Xu, Q.; et al. Enhancement of Two-Photon Fluorescence and Low Threshold Amplification of Spontaneous Emission of Zn-Processed CuInS2 Quantum Dots. *ACS Photonics* **2018**, *5*, 1310–1317. https://doi.org/10.1021/acsphotonics.7b01255.

(15) Shabaev, A.; Mehl, M. J.; Efros, A. L. Energy Band Structure of CuInS2 and Optical Spectra of CuInS2 Nanocrystals. *Phys. Rev. B - Condens. Matter Mater. Phys.* **2015**, *92*, 1–9. https://doi.org/10.1103/PhysRevB.92.035431.

(16) Knowles, K. E.; Hartstein, K. H.; Kilburn, T. B.; Marchioro, A.; Nelson, H. D.; Whitham, P. J.; Gamelin, D. R. Luminescent Colloidal Semiconductor Nanocrystals Containing Copper: Synthesis, Photophysics, and Applications. *Chem. Rev.* **2016**, *116*, 10820–10851. https://doi.org/10.1021/acs.chemrev.6b00048.

(17) Leach, A. D. P.; Macdonald, J. E. Optoelectronic Properties of CuInS2 Nanocrystals and Their Origin. *J. Phys. Chem. Lett.* **2016**, *7*, 572–583. https://doi.org/10.1021/acs.jpclett.5b02211.

(18) Nagamine, G.; Nunciaroni, H. B.; Mcdaniel, H.; Efros, A. L.; De Brito Cruz, C. H.; Padilha, L. A. Evidence of Band-Edge Hole Levels Inversion in Spherical CuInS2 Quantum Dots. *Nano Lett.* **2018**, *18*, 6353–6359. https://doi.org/10.1021/acs.nanolett.8b02707.

(19) Anand, A.; Zaffalon, M. L.; Gariano, G.; Camellini, A.; Gandini, M.; Brescia, R.; Capitani, C.; Bruni, F.; Pinchetti, V.; Zavelani-Rossi, M.; et al. Evidence for the Band-Edge Exciton of CuInS2 Nanocrystals Enables Record Efficient Large-Area Luminescent Solar Concentrators. *Adv. Funct. Mater.* **2020**, *30*, 1–13. https://doi.org/10.1002/adfm.201906629.

(20) Pinchetti, V.; Lorenzon, M.; McDaniel, H.; Lorenzi, R.; Meinardi, F.; Klimov, V. I.; Brovelli, S. Spectro-Electrochemical Probing of Intrinsic and Extrinsic Processes in Exciton Recombination in I-III-VI2 Nanocrystals. *Nano Lett.* **2017**, *17*, 4508–4517. https://doi.org/10.1021/acs.nanolett.7b02040.

(21) Maiti, S.; Dana, J.; Jadhav, Y.; Debnath, T.; Haram, S. K.; Ghosh, H. N. Electrochemical Evaluation of Dopant Energetics and the Modulation of Ultrafast Carrier Dynamics in Cu-Doped CdSe Nanocrystals. *J. Phys. Chem. C* **2017**, *121*, 27233–27240. https://doi.org/10.1021/acs.jpcc.7b10262.

(22) Knowles, K. E.; Nelson, H. D.; Kilburn, T. B.; Gamelin, D. R. Singlet-Triplet Splittings in the Luminescent Excited States of Colloidal Cu+:CdSe, Cu+:InP, and CuInS2 Nanocrystals: Charge-Transfer Configurations and Self-Trapped Excitons. *J. Am. Chem. Soc.* **2015**, *137*, 13138–13147. https://doi.org/10.1021/jacs.5b08547.

(23) Yang, L.; Knowles, K. E.; Gopalan, A.; Hughes, K. E.; James, M. C.; Gamelin, D. R. One-Pot Synthesis of Monodisperse Colloidal Copper-Doped CdSe Nanocrystals Mediated by Ligand-Copper Interactions. *Chem. Mater.* **2016**, *28*, 7375–7384. https://doi.org/10.1021/acs.chemmater.6b02869.

(24) Hughes, K. E.; Hartstein, K. H.; Gamelin, D. R. Photodoping and Transient Spectroscopies of Copper-Doped CdSe/CdS Nanocrystals. *ACS Nano* **2018**, *12*, 718–728. https://doi.org/10.1021/acsnano.7b07879.

(25) Fuhr, A.; Yun, H. J.; Crooker, S. A.; Klimov, V. I. Spectroscopic and Magneto-Optical Signatures of Cu1+ and Cu2+ Defects in Copper Indium Sulfide Quantum Dots. *ACS Nano* **2020**, *14*, 2212–2223. https://doi.org/10.1021/acsnano.9b09181.

(26) Fuhr, A.; Alexandrova, A.; Sautet, P. Stoichiometry-Controllable Optical Defects in Cu x In 2-x S y Quantum Dots for Energy Harvesting. *J. Mater. Chem. A* **2020**, *8*, 12556–12565. https://doi.org/10.1039/d0ta03954c.

(27) Van Der Stam, W.; De Graaf, M.; Gudjonsdottir, S.; Geuchies, J. J.; Dijkema, J. J.; Kirkwood, N.; Evers, W. H.; Longo, A.; Houtepen, A. J. Tuning and Probing the Distribution of Cu+ and Cu2+ Trap States Responsible for Broad-Band Photoluminescence in CuInS2 Nanocrystals. *ACS Nano* **2018**, *12*, 11244–11253. https://doi.org/10.1021/acsnano.8b05843.

(28) Xiang, W.; Ma, X.; Luo, L.; Cai, W.; Xie, C.; Liang, X. Facile Synthesis and Characterization of Core/Shell Cu-In-Zn-S/ZnS Nanocrystals with High Luminescence. *Mater. Chem. Phys.* **2015**, *149*, 437–444. https://doi.org/10.1016/j.matchemphys.2014.10.042.

(29) Nelson, H. D.; Gamelin, D. R. Valence-Band Electronic Structures of Cu+ -Doped ZnS, Alloyed Cu-In-Zn-S, and Ternary CuInS2 Nanocrystals: A Unified Description of Photoluminescence across Compositions. *J. Phys. Chem. C* **2018**, *122*, 18124–18133. https://doi.org/10.1021/acs.jpcc.8b05286.

(30) Moser, A.; Yarema, M.; Lin, W. M. M.; Yarema, O.; Yazdani, N.; Wood, V. In Situ Monitoring of Cation-Exchange Reaction Shell Growth on Nanocrystals. *J. Phys. Chem. C* **2017**, *121*, 24345–24351. https://doi.org/10.1021/acs.jpcc.7b08571.

(31) Vale, B. R. C.; Socie, E.; Burgos-Caminal, A.; Bettini, J.; Schiavon, M. A.; Moser, J. E. Exciton, Biexciton, and Hot Exciton Dynamics in CsPbBr3 Colloidal Nanoplatelets. *J. Phys. Chem. Lett.* **2020**, *11*, 387–394. https://doi.org/10.1021/acs.jpclett.9b03282.

(32) Li, L.; Pandey, A.; Werder, D. J.; Khanal, B. P.; Pietryga, J. M.; Klimov, V. I. Efficient Synthesis of Highly Luminescent Copper Indium Sulfide-Based Core/Shell Nanocrystals with Surprisingly Long-Lived Emission. *J. Am. Chem. Soc.* **2011**, *133*, 1176–1179.

https://doi.org/10.1021/ja108261h.

(33) Debnath, T.; Maiti, S.; Maity, P.; Ghosh, H. N. Subpicosecond Exciton Dynamics and Biexcitonic Feature in Colloidal CuInS2 Nanocrystals: Role of In-Cu Antisite Defects. *J. Phys. Chem. Lett.* **2015**, *6*, 3458–3465. https://doi.org/10.1021/acs.jpclett.5b01767.

(34) Debnath, T.; Ghosh, H. N. Ternary Metal Chalcogenides: Into the Exciton and Biexciton Dynamics. *J. Phys. Chem. Lett.* **2019**, *10*, 6227–6238. https://doi.org/10.1021/acs.jpclett.9b01596.

(35) Guo, Y.; Yang, F.; Zheng, X.; Tang, J.; Zhong, H.; Yu, A.; Wang, J.; Zou, B. Direct Observation of Surface Polarons in Capped CuInS2 Quantum Dots by Ultrafast Pump-Probe Spectroscopies. *J. Phys. Chem. Lett.* **2019**, *10*, 5297–5301. https://doi.org/10.1021/acs.jpclett.9b02023.

Supporting Information

Revealing Exciton and Metal-Ligand Conduction Band Charge Transfer Absorption Spectra in Cu-Zn-In-S Nanocrystals

Brener R. C. Vale,[†§] *Etienne Socie,*[†] *Leticia R. C. Cunha,*[§] *Andre F. V. Fonseca,*[§] *Roberto Vaz,*[§] *Jefferson Bettini,*[‡] *Jacques-E. Moser,*[†*] *Marco A. Schiavon*[§*]

[†] Photochemical Dynamics Group, Institute of Chemical Sciences & Engineering, École Polytechnique Fédérale de Lausanne, CH-1015 Lausanne, Switzerland

[§] Grupo de Pesquisa Química de Materiais, Departamento de Ciências Naturais, Universidade Federal de São João Del-Rei, Campus Dom Bosco, 36301-160 São João Del-Rei, Minas Gerais, Brazil

[‡] Laboratório Nacional de Nanotecnologia, Centro Nacional de Pesquisa em Energia e Materiais, Campinas, São Paulo, Brazil

1. Methods

Chemicals and Materials. All chemicals were used as received without further purification. Indium chloride ($InCl_3 \cdot 4H_2O$, 97%), Copper Iodide (CuI, 99.5%), n-dodecanethiol (DDT, 98%), oleic acid (OA, 90%), oleylamine (OAm, 70%), 1-octadecene (ODE, 90%) and Acetone (99%) were purchased from Sigma-Aldrich. Toluene (99%) and Zinc chloride ($ZnCl_2$, 97%), were purchased from Exodos Científica, and Dinâmica Química, respectively.

Synthesis of CZIS QDs: We prepared CZIS QDs by following a previous procedure described in the literature with slight modification. First, we prepared a solution containing all the metals and

the ligands. Briefly, we reacted 0.2 mmol $ZnCl_2$, 0.2 mmol $InCl_3$, 0.04 mmol CuCl and 60 µL of oleic acid, 250 µL of DDT dissolved in 8 mL of ODE in a 25 mL three-necked flask. The solution was heated to 90 ºC under vacuum with magnetic stirring for 30 minutes. Then, we heated the system under argonium gas flow until 180 ºC for 5 minutes. Second, we reacted the metal solution with sulfur solution. This step was performed by dropping the temperature to 160 ºC and added a mixture of 0.8 mmol S dispersed in 2 mL of OAm into the three-necked flask containing all the metals and reacting for 10 minutes to allow the growth of CZIS QDs.

Cation-exchange with Zn^{2+}: To perform the cation-exchange reaction, we first prepared a Zn stock solution by dissolving 2.0 mmol $ZnCl_2$ and 1 mL of OAm in 4 mL of ODE into a three-necked flask. The reaction mixture was heated to 90 ºC under Argonium flow with magnetic stirring for 30 minutes. After that, the flask was heated to 150 ºC for 10 minutes to obtain a clear solution. Next, we cooled down the temperature to 50 ºC for further use. For CZIS/ZnS 100 and CZIS/ZnS 200 QDs, we used the CZIS QDs prepared as described above without purification step. Then, we injected the Zn stock solution with a syringe into CZIS QDs at 100 and 200 ºC for CZIS/ZnS 100 and CZIS/ZnS 200, respectively, for 30 minutes. For the purification step, we added acetone until the solution gets turbid. Next, we centrifuged it at 7000 rpm for 10 minutes. Finally, we discard the supernatant and dissolve the precipitate containing the QDs in 3 mL of Toluene. We could prepare QDs that were stable for months by following this procedure.

Characterization. Steady-state fluorescence spectra were collected on a Horiba Jobin Yvon Fluorolog-3 fluorometer equipped with a Xe lamp of 450 W. The excitation wavelength was set to 390 nm. For TCSPC analysis, we used a nanoLED as a pulsed source with a central wavelength at 390 nm. We used a 1.00 MHz repetition rate, with a resolution of 212 ps and an instrument response function (IRF) width of 1.3 ± 0.1 ns. Detection was performed at 90º relative to the excitation source. Ultraviolet-visible absorption spectra were acquired on a Perkin Elmer Lambda 950 UV/Vis/NIR spectrometer. The fluorescence and absorption spectra in the steady state were acquired by using cuvettes with an optical path of 10.00 mm. For transient absorption spectroscopy, we used cuvettes with an optical path of 1.00 mm.

Ultrafast transient absorption spectra of all samples were obtained using a fs chirped pulse amplified (CPA) Ti:sapphire laser (Clark-MXR, CPA-2001). The pump beam at 390 nm was obtained by frequency doubling the fundamental output of the laser (778 nm, 120 fs pulse duration,

1 kHz repetition rate) in a 0.5 mm-thick BBO crystal. The pump beam at 500 nm was obtained by directing the CPA output into a non-linear parametric amplifier (NOPA), with subsequent compression to 60 fs pulse duration with a pair of SF10 prisms. The probe beam was produced by focusing a portion of the fundamental of the laser into a oscillating CaF_2 crystal, yielding a white light continuum spanning from 400 to 780 nm. The probe light used in all experiments had a smaller beam cross section and a weaker intensity compared to the pump beam as to obtain a homogenous probed area. The pump beam was chopped at 500 Hz. The dynamics of the photoinduced spectra were determined using a digitally controlled delay stage (PI) in the pump path. The polarization of the pump compared to the probe was set to magic angle (54.6º) to consider only population dynamics. The probe beam was split before the sample into reference and a signal branches, with the latter going through the sample, and both were separately sent into respective spectrographs (Princeton Instruments, Spectra Pro 2150i) and detected shot-to-shot by CCD cameras (Hamamatsu S07030-0906). The time resolution of the experiment was calculated to be 300 fs whem pumped at 390, or less than 100 fs whem pumped at 500 nm.

PLQY Measurements. We carried out PLQY measurements by a relative method, using a dye with a known PLQY. In this case, we have used Rhodamine 6G diluted in ethanol as a standard with PLQY of 92%. We recorded the PL spectrum and absorption at the same wavelength used to excite the samples at 355 nm. We measured at least six different concentrations for each sample in the absorbance range of 0.006 – 0.1. A graph of PL integrated area *versus* absorbance at 355 nm was plotted and a linear fit of the data was applied.

$$\Phi_x = \Phi_{st}\left(\frac{Slope_x}{Slope_{st}}\right)\left(\frac{\eta_x^2}{\eta_{st}^2}\right) \quad \text{S1}$$

Slope refers to the angular coefficient of the curves obtained, η is the refractive index of the medium. Where x, st and Φ refer to sample, standard, and PLQY, respectively. Since the prepared solutions were very diluted, we assumed that the refractive index was very close to the pure solvent.

2. Global Analysis

The fitting procedure in this work was carried out using a multiple exponential function with a global fitting, in which all the time constants were linked to each other depending on the wavelength. Global analysis was employed to assess the dynamics and spectral features from band-edge exciton absorption and hole localization into CHS. We extracted the kinetic traces every 5 nm from 450 to 700 nm, and we fitted the data from 0.6 to 1880 ps when pumped at 390 nm. For the samples pumped at 500 nm, we extracted the

kinetic traces by averaging them into 5 different wavelength every 10 nm from 510 to 725 nm, and we fitted the data from 0.14 to 1880 ps. Finally, we extracted the amplitude coefficients ($A_i(\lambda)$) for each time constant (τ_1, τ_2, and τ_3) as $A_1(\lambda)$, $A_2(\lambda)$, and $A_3(\lambda)$ for each trace and plotted the amplitude *versus* wavelength.

$$\Delta A\,(\lambda, t) = \sum_i^3 A_i exp\left(\frac{-t}{\tau_i}\right) \quad \text{S2}$$

$$\Delta A\,(\lambda, t) = y_0 + \sum_i^3 A_i exp\left(\frac{-t}{\tau_i}\right) \quad \text{S3}$$

Equation S2 and S3 were used for samples pumped at 390 nm and at 500 nm, respectively.

3. Absorption Cross-section Measurements

We have used a procedure based on Poisson statistics that is well-described and used for different semiconductors QDs in the literature.[1–3] The probability of having n excitons per QD is given by Eq. S4.

$$P(n) = \frac{\langle N_x\rangle^n . \exp\left(-\langle N_x\rangle\right)}{n!} \quad \text{S4}$$

Where $<N_x>$ is the average exciton per particle, which is equal to the product of the absorption cross-section at the specific pump energy at 3.2. eV ($\sigma_{3.2\ eV}$), and the density of photon per pulse per area (j), Eq S5.

$$\langle N_x\rangle = \sigma_{3.2\ eV} j \quad \text{S5}$$

After a long time delay such as larger than 1000 ps, all biexcitons which contributes twice to the signal have already decayed via Auger recombination, so that only one exciton per particle is present, which contributes once to the signal, independent on the initial number of excitons created. This can be modeled by Eq. S6:

$$\Delta A = A[1 - P(0)] = A(1 - \exp(-< N_x >)) \quad \text{S6}$$

Since the $\sigma_{3.2\ eV}$ is a constant, we can find it by measuring the amplitude of the GSB at 1880 ps in function of the photofluences. Thus, we have fitted our experimental data with Eq S6. The results for the three samples are shown in Fig. 1S.

Because of our pump fluence at 500 nm (2.48 eV) was not enough to saturate the TA signal of the samples, we measured the absorption cross-section at 390 nm. Since the absorption cross-section dependent on the wavelength is proportional to the absorbance, we used the absorption spectra to calculate $\sigma_{2.48\ eV}$. Fig. 2S shows the estimated cross-section absorption spectra for CZIS, CZIS/ZnS 100, and CZIS/ZnS 200.

Table S1: PL maximum and second order derivative absorption minimum of the UV-Vis spectra

Sample	PL/nm	UV-Vis/ nm	PL/eV	UV-Vis/eV	Apparent Stokes/eV
CZIS	661	550	1.876	2.254	0.378
CZIS/ZnS100	614	523	2.019	2.371	0.352
CZIS/ZnS200	586	516	2.116	2.403	0.287

Table S2: TA bleach peak minimum and true Stokes shift and difference between TA bleach minimum and band-gap

Sample	TA Bleach peak/ eV	True Stokes / eV	Δ(CHS – BG) / eV
CZIS	2.157	0.281	0.097
CZIS/ZnS100	2.288	0.270	0.083
CZIS/ZnS200	2.340	0.224	0.063

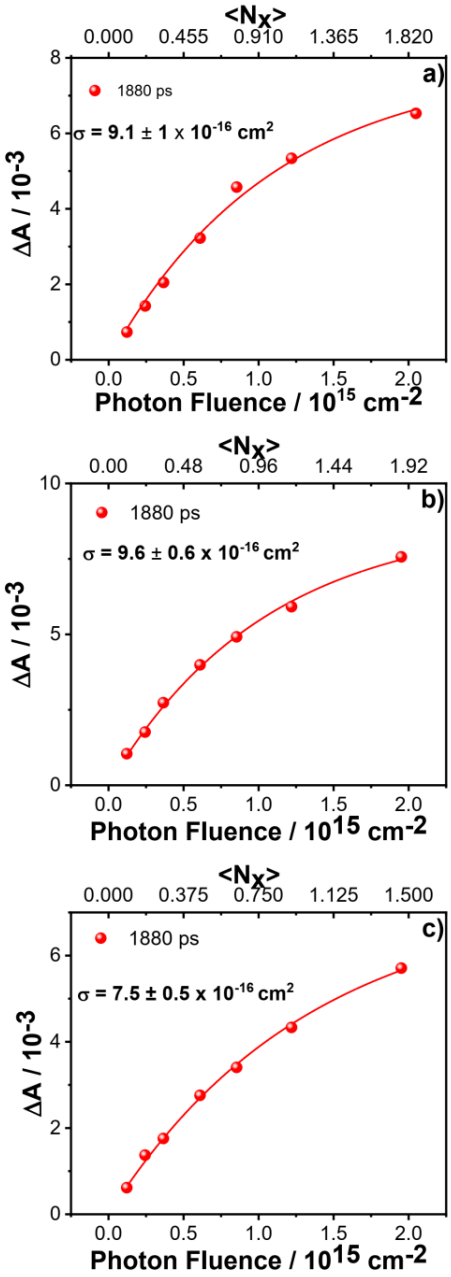

Fig. 1S: Dependence of TA bleaching on the photon fluence at 1880 ps to extract the absorption cross-section at 3.2 eV of a) CZIS, b) CZIS/ZnS 100, and c) CZIS/ZnS 200.

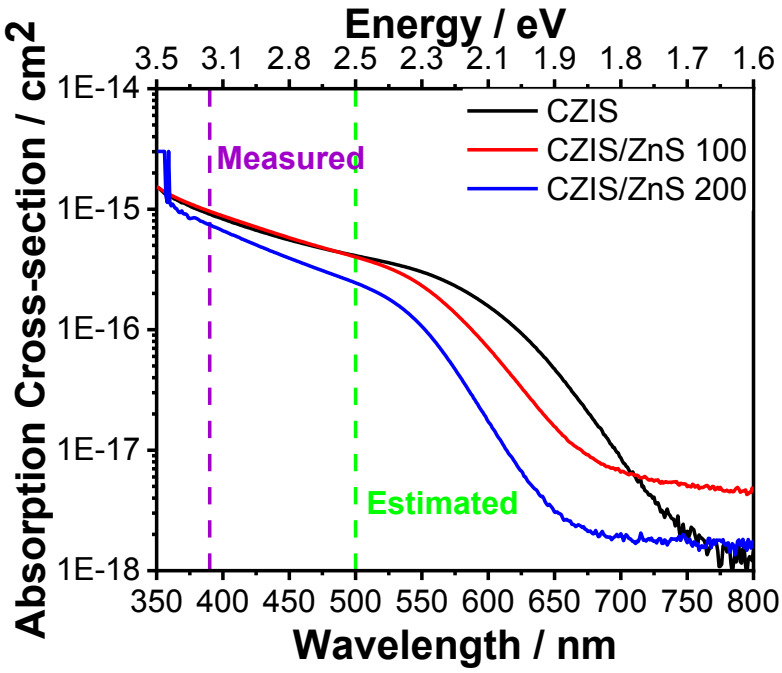

Fig. 2S: Estimated absorption cross-section spectra for CZIS, CZIS/ZnS 100, and CZIS/ZnS 200. The purple and green dashed lines show the measured and estimated absorption cross-section. In log scale is clear the suppression of the absorption band between 600 to 800 nm from CZIS to CZIS/ZnS 200 QDs. We found $\sigma_{.248\ eV}$ to be 4.1 x 10^{-16}, 4.0 x 10^{-16}, 2.5 x 10^{-16} cm^2 for CZIS, CIZS/ZnS 100, and CZIS/ZnS 200, respectively.

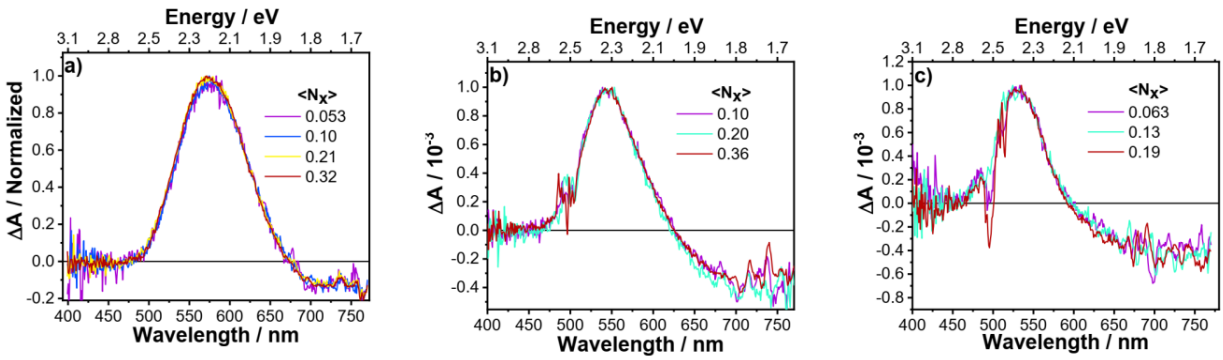

Fig. 3S: TA spectra normalized at 1 ps with different photon fluence for a) CZIS, b) CZIS/ZnS 100, c) CZIS/ZnS 200

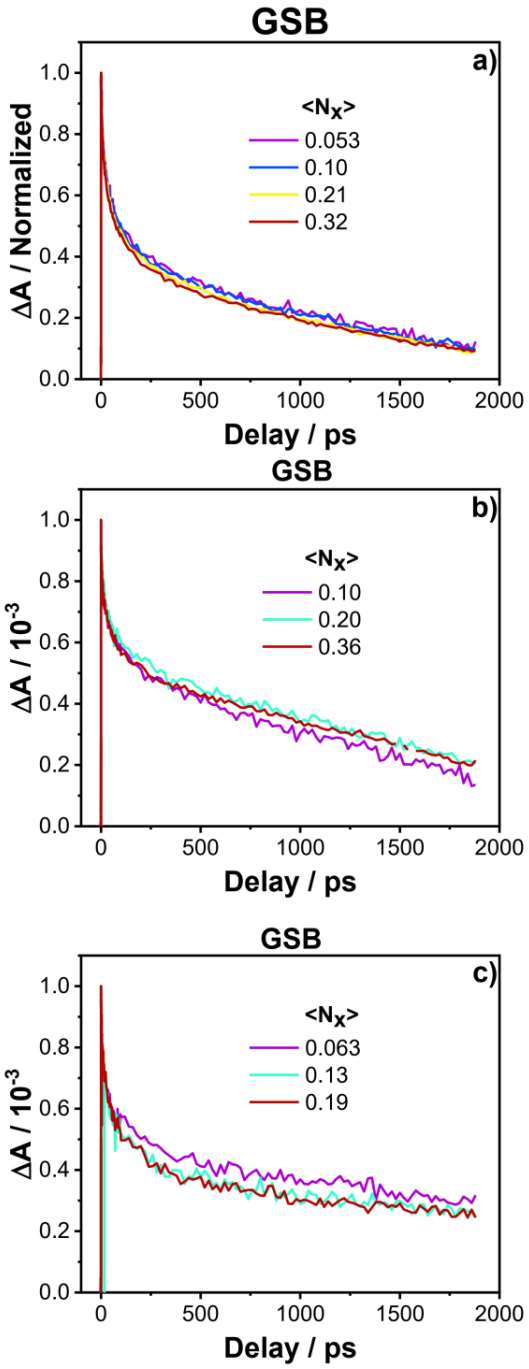

Fig.4S: GSB decay at different photofluence for a) CZIS, b) CZIS/ZnS 100, and c) CZIS/ZnS 200

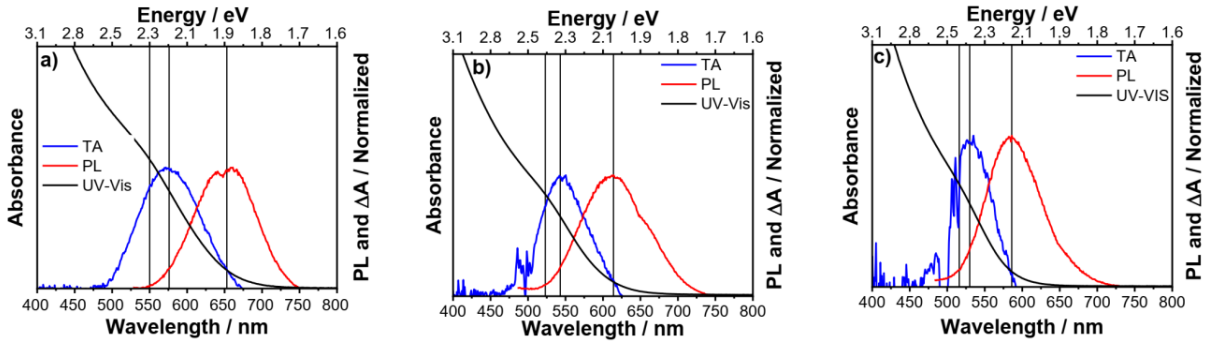

Fig. 5S: TA, PL, and UV-Vis spectra of a) CZIS, b) CZIS/ZnS 100, and c) CZIS/ZnS 200.

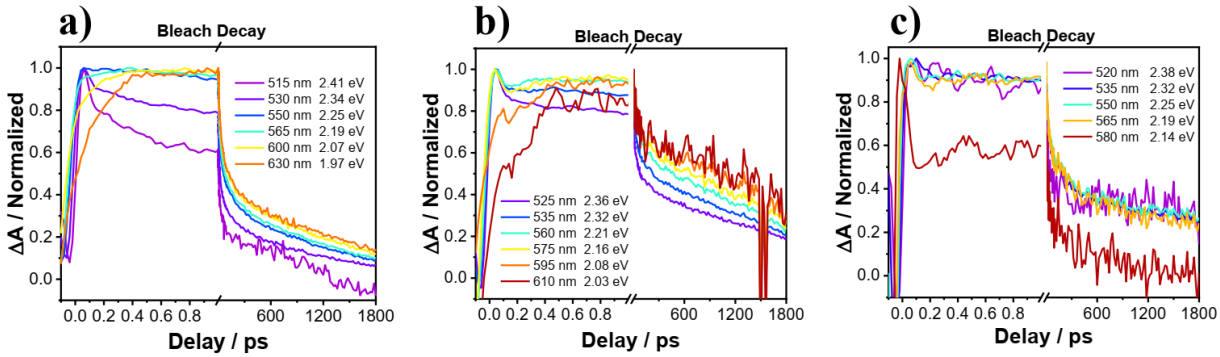

Fig. 6S: Decay curves probed at different energies pumped at 500 nm for a) CZIS, b) CZIS/ZnS 100, C) CZIS/ZnS 200. The curves were normalized to 1 at its maximum signal.

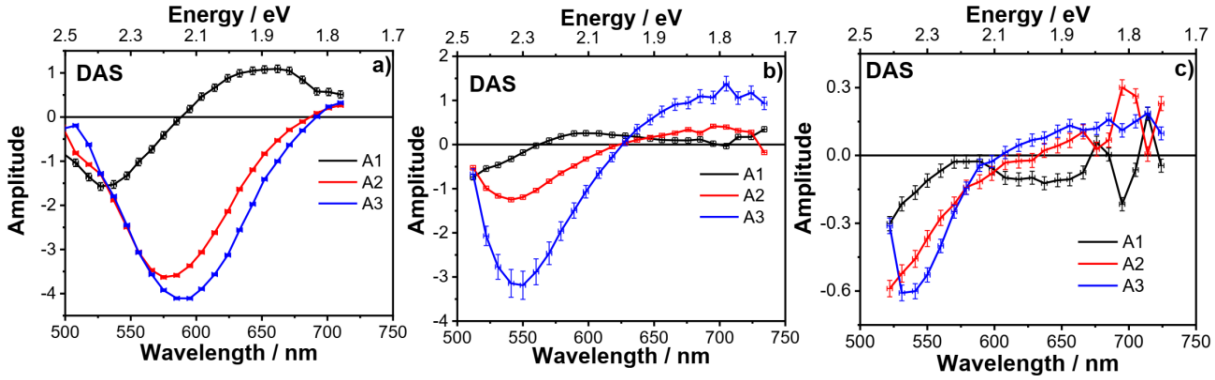

Fig. 7S: DAS pumped at 500 nm for a) CZIS, b) CZIS/ZnS 100, c) CZIS/ZnS 200

Table S3: Time-constant for DAS pumped at 500 nm

Sample	τ_1 (ps)	τ_2 (ps)	τ_3 (ps)
CZIS	0.31 ± 0.01	21.4 ± 0.3	1290 ± 12
CZIS/ZnS 100	0.91 ± 0.1	31 ± 2	2327 ± 350
CZIS/ZnS 200	1.7 ± 0.2	30 ± 3	3500± 400

Table S4: Time-constant for DAS pumped at 390 nm

Sample	τ_1 (ps)	τ_2 (ps)	τ_3 (ps)
CZIS	4.7 ± 0.2	78 ± 2	3379 ± 118
CZIS/ZnS 100	4.7 ± 0.4	157 ± 16	6407 ± 511
CZIS/ZnS 200	17.5 ± 0.8	390 ± 29	32776 ± 5000

Table S5: PL decay time constants and radiative and nonradiative lifetime

Sample	τ_1 / ns	τ_2 / ns	τ_r / ns	τ_{nr} / ns	$<\tau>$ / ns
CZIS	13.2 ± 0.1 (0.54)	125 ± 0.6 (0.40)	926	126	111
CZIS/ZnS 100	15.5 ± 0.2 (0.42)	142 ± 0.5 (0.50)	781	160	133
CZIS/ZnS 200	13.1 ± 0.1 (0.44)	125 ± 0.5 (0.46)	212	250	115

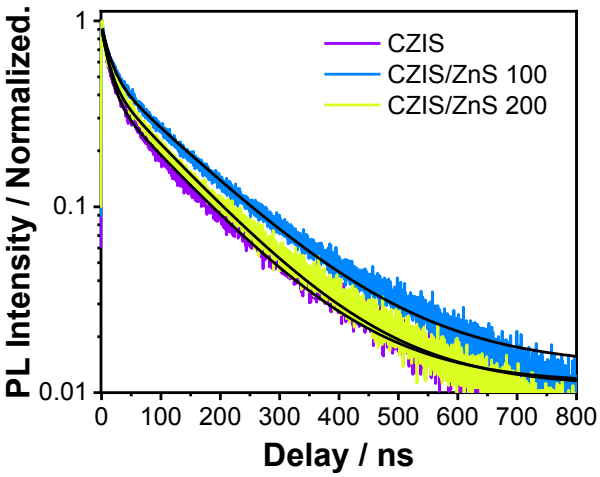

Fig. 8S: PL decay curve for CZIS, CZIS/ZnS 100, and CZIS/ZnS 200 obtaining from TCSPC technique.

The average PL lifetime was measured by Eq. S7. A PL lifetime constant is defined as a reciprocal of the radiative and nonradiative rate, k_r and k_{nr}, respectively. Combining Equation S8 and S9 we can find k_r and k_{nr}.

$$< \tau > = \frac{A_1\tau_1^2 + A_2\tau_2^2}{A_1\tau_1 + A_2\tau_2} \quad \text{S7}$$

$$< \tau > = \frac{1}{k_r + k_{nr}} \quad \text{S8}$$

$$\Phi = \frac{k_r}{k_r + k_{nr}} \quad \text{S9}$$